

Structure and Gelation Mechanism of Tunable Guanosine-Based  
Supramolecular HydrogelsZheng Li,<sup>†</sup> Lauren E. Buerkle,<sup>†</sup> Maxwell R. Orseno,<sup>‡</sup> Kiril A. Streltzky,<sup>‡</sup> Soenke Seifert,<sup>§</sup>  
Alexander M. Jamieson,<sup>\*,†</sup> and Stuart J. Rowan<sup>†</sup><sup>†</sup>Department of Macromolecular Science and Engineering, Case Western Reserve University, Cleveland, Ohio 44106, <sup>‡</sup>Department of Physics, Cleveland State University, Cleveland, Ohio 44115, and <sup>§</sup>Advanced Photon Source, Argonne National Laboratory, Argonne, Illinois 60439

Received January 15, 2010. Revised Manuscript Received March 17, 2010

The mechanism of gelation of 50/50 w/w mixtures of guanosine (**G**) and 2',3',5'-tri-*O*-acetylguanosine (**TAcG**) in aqueous 0.354 M KCl was investigated using a combination of static light scattering (SLS), polarized and depolarized dynamic light scattering (VV and VH DLS), small-angle neutron and X-ray scattering (SANS and SAXS), and viscometric experiments. SLS and viscometry show a dramatic increase in apparent molecular weight and hydrodynamic volume at 0.2 wt % and 0.3 wt %, respectively, indicating the critical concentration for self-association of **G/TAcG** quartets into columnar assemblies lies below 0.2 wt %. Above this concentration, SANS and SAXS generate complementary information on the structure of the individual columnar stacks. VV and VH DLS results indicate bimodal correlation functions, whose properties suggest, respectively, translational and rotational diffusion of a bimodal distribution of particles. The fast mode appears to originate from fibrillar agglomerates of **G/TAcG** columnar quartet assemblies, while the slow mode comes from microgel domains. Guinier plot analysis of the SLS data probes the internal structure of the microgel domains. Collectively, the results suggest that sol and microgel phases coexist below the macroscopic gel point, and that the sol phase contains individual columnar stacks of **G/TAcG** quartets and fibrillar aggregates formed via lateral aggregation of these columnar assemblies. With increasing concentration, the DLS data indicate a progressive increase in the volume fraction of microgel domains, which ultimately leads to macroscopic gelation. Prior observation of a transient network contribution to the gel rheology at low temperature is attributed to the presence of individual columnar stacks within the gel network.

## Introduction

Supramolecular hydrogels are attracting increasing attention because of their potential applications in different fields such as tissue engineering,<sup>1</sup> stimuli-responsive materials,<sup>2,3</sup> and sensors.<sup>4–6</sup> Supramolecular architectures have been generated via self-assembly of guanosine derivatives.<sup>7–9</sup> In the presence of certain metal ions, such as potassium or sodium ions, guanosine derivatives self-assemble<sup>8</sup> into planar cyclic quartets, which then can associate further into columnar stacks. One problem with hydrogels formed by guanosine and a number of its derivatives is their limited lifetime stability on account of crystallization. Yu et al.<sup>10</sup> reported stable gels can be obtained in KCl/Tris buffer solution by mixing guanosine (**G**) and guanosine 5'-monophosphate (**GMP**). Recently, stable and transparent hydrogels were prepared by mixing guanosine (**G**) with a nongelator of similar structure,

namely 2',3',5'-tri-*O*-acetylguanosine (**TAcG**) (Figure 1).<sup>11</sup> The thermomechanical properties of the resulting hydrogels can be tuned by changing the ratio between **G** and **TAcG**. Atomic force microscopy (AFM) studies confirmed the formation of fibrillar structures in these gels, and small angle neutron scattering (SANS) measurements of hydrogels at three compositions in the gelation composition range were accurately described by a core-shell cylinder model,<sup>11</sup> which reflects the fact that the labile hydrogens in the interior of the **G/TAcG** quartets are substituted by deuterium, resulting in an axial gradation in scattering density length. An apparent cylinder length decrease with increase in **TAcG** content was observed, which correlated with a decrease in gel modulus, and is consistent with the expectation that **TAcG** will inhibit the elongation of the cylinders. The AFM studies,<sup>11</sup> performed on dried gel specimens, deposited on a freshly cleaved mica substrate, indicate a fibrous network of thicknesses substantially larger than the width of the columnar stacks of **G/TAcG** quartets (ca. 3 nm), suggesting that the columnar stacks laterally associate into fibers.

Knowledge of the self-assembly and gelation mechanism of supramolecular hydrogels is critical to understanding how to tune their properties. The motivation for the present work is to generate information on the mechanistic steps by which the supramolecular aggregates are formed, and hence gain more insight into the gelation mechanism. This has been accomplished by complementing our earlier SANS and AFM studies with static light scattering (SLS), polarized and depolarized dynamic light

\*Corresponding author.

(1) Wu, D. Q.; Wang, T.; Lu, B.; Xu, X. D.; Cheng, S. X.; Jiang, X. J.; Zhang, X. Z.; Zhuo, R. X. *Langmuir* **2008**, *24*, 10306–10312.

(2) Matsumoto, S.; Yamaguchi, S.; Ueno, S.; Komatsu, H.; Ikeda, M.; Ishizuka, K.; Iko, Y.; Tabata, K. V.; Aoki, H.; Ito, S.; Noji, H.; Hamachi, I. *Chem.—Eur. J.* **2008**, *14*, 3977–3986.

(3) Komatsu, H.; Matsumoto, S.; Tamaru, S.; Kaneko, K.; Ikeda, M.; Hamachi, I. *J. Am. Chem. Soc.* **2009**, *131*, 5580–5585.

(4) Yamaguchi, S.; Yoshimura, L.; Kohira, T.; Tamaru, S.; Hamachi, I. *J. Am. Chem. Soc.* **2005**, *127*, 11835–11841.

(5) Koshi, Y.; Nakata, E.; Yamane, H.; Hamachi, I. *J. Am. Chem. Soc.* **2006**, *128*, 10413–10422.

(6) Wada, A.; Tamaru, S.; Ikeda, M.; Hamachi, I. *J. Am. Chem. Soc.* **2009**, *131*, 5321–5330.

(7) Davis, J. T. *Angew. Chem., Int. Ed.* **2004**, *43*, 668–698.

(8) Davis, J. T.; Spada, G. P. *Chem. Soc. Rev.* **2007**, *36*, 296–313.

(9) Sivakova, S.; Rowan, S. J. *Chem. Soc. Rev.* **2005**, *34*, 9–21.

(10) Yu, Y.; Nakamura, D.; DeBoyace, K.; Niesius, A. W.; McGown, L. B. *J. Phys. Chem. B* **2008**, *112*, 1130–1134.

(11) Buerkle, L. E.; Li, Z.; Jamieson, A. M.; Rowan, S. J. *Langmuir* **2009**, *25*, 8833–8840.

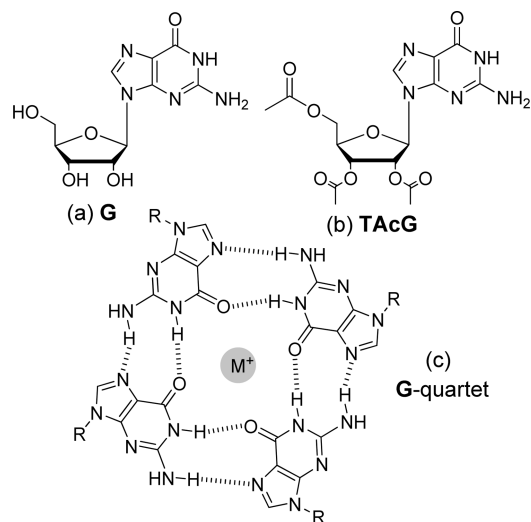


**Figure 1.** Structures of (a) guanosine (**G**), (b) 2',3',5'-tri-*O*-acetyl-guanosine (**TAcG**), and (c) a G-quartet.

scattering (DLS), synchrotron small-angle X-ray scattering (SAXS) and viscosity experiments performed on **G/TAcG** mixtures in aqueous 0.354 M KCl over a range of concentrations encompassing the gelation transition.

Prior investigations of the self-aggregation behavior of sodium, potassium and ammonium salts of guanosine 5'-monophosphate (**GMP**) and deoxyguanosine 5'-monophosphate (**DGMP**) in aqueous solution have been reported, employing DLS, NMR, and SAXS.<sup>12–17</sup> Small rodlike aggregates composed of guanosine quartet stacks were found in solution. In concentrated KCl solution, cylinders of **DGMP** were found to associate into a hexagonal phase.<sup>17</sup> Analogous to our AFM images of **G/TAcG** gels, SEM images of **GMP** in alkali metal salts display long straight or curved rods composed of bundles of stacks of guanosine quartets.<sup>18</sup> By way of contrast, we note that **G/TAcG** mixtures gel at much lower concentrations (0.8 wt %) than **GMP** or **DGMP**, and so our experiments are necessarily carried out at higher dilutions than these earlier experiments.

## Results and Discussion

A 50/50 **G/TAcG** ratio was chosen to investigate the process of gel formation. From previous dynamic light scattering (DLS) data,<sup>11</sup> the gel point was found to occur at a concentration of around 0.8 wt %. Thus, a concentration series of 50/50 **G/TAcG** in the range 0.05–1 wt % as well as a 2 wt % gel were prepared for characterization using scattering techniques and viscometry.

**Small Angle Neutron Scattering (SANS).** In our previous publication, the SANS scattering profile of a 2 wt % **G/TAcG** gel was presented and briefly discussed.<sup>11</sup> Here, we have completed further analysis of that data in order to gain more insight into the architecture of the gel. In Figure 2 these data are replotted in the form of a Holtzer plot, i.e.,  $\log qI(q)$  versus  $\log q$ . The plateau

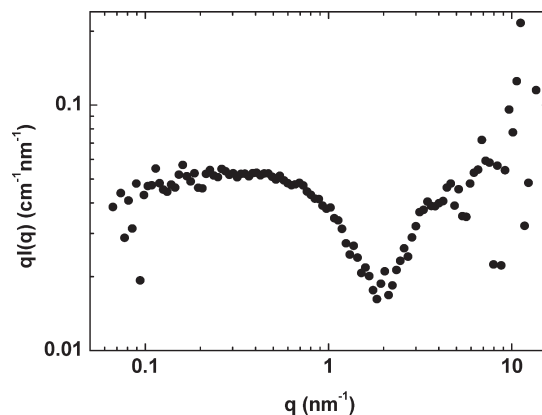


**Figure 2.** Holtzer plot ( $\log qI(q)$  versus  $\log q$ ) of SANS scattering from 2 wt % **G/TAcG** 50/50 gel in 0.354 M aqueous KCl. Both the plateau regime in the intermediate  $q$  range (0.12–0.6  $\text{nm}^{-1}$ ) and the sharp decay and subsequent increase of intensity at large  $q$  are characteristic indicators that long rigid-rod segments exist in the gel.

regime in the intermediate  $q$  range (0.12–0.6  $\text{nm}^{-1}$ ) is a characteristic indicator that the scattered intensity decays as  $I(q) \sim q^{-1}$ , i.e., that long rigid-rod segments exist in the gel. This conclusion is further evident in a plot of  $\log(I(q))$  versus  $\log(q)$  (see Supporting Information). In Figure 2, the sharp decay and subsequent increase of intensity at large  $q$  reflects diffractive scattering from the rod cross-section, and thus is also emblematic of the presence of a rigid rod structure.<sup>19–21</sup>

As noted by Buhler et al.<sup>21</sup> the scattered intensity in the plateau regime of the Holtzer plot (Figure 2: 0.12–0.6  $\text{nm}^{-1}$ ) can be described by  $I(q) \sim (\Delta\rho)^2 \times M_L \times \pi/q$ ,<sup>21,22</sup> which enables a determination of  $M_L$ , the molecular weight per unit length of the columnar stacks of **G/TAcG** quartets. Specifically, the scattered intensity can be expressed as the sum of a form factor  $P(q)$  and a structure factor  $S(q)$  as indicated in eq 1:

$$I(q) = (\Delta\rho)^2 \phi_{\text{vol}} V_{\text{chain}} P(q) S(q) \quad (1)$$

where  $V_{\text{chain}}$  is the volume of one chain (rod). We neglect  $S(q)$ , which reflects inter-rod interferences, and write  $P(q)$  as

$$P(q) = \frac{\pi}{qL_c} + \frac{2}{3q^2 L_T L_c} \quad (2)$$

where  $L_c$  is the contour length of the rods, and  $L_T$  is the total persistence length (i.e., the sum of the conformational and electrostatic contributions). In the intermediate  $q^{-1}$  range, the second term in eq 2 can also be neglected. Hence, inserting eq 2 into eq 1, we obtain eq 3

$$I(q) = \frac{\pi \phi_{\text{vol}} (\Delta\rho)^2 M_L}{N_A \delta q} \quad (3)$$

where  $N_A$  is Avogadro's number,  $\delta$  is the density of the gelator, and we have used the relationships  $V_{\text{chain}} = M_n/\delta$ , where  $M_n$  is the number-average molecular weight of the rod, and  $M_L = M_n/L_c$ .

(12) Mariani, P.; Mazabard, C.; Garbesi, A.; Spada, G. P. *J. Am. Chem. Soc.* **1989**, *111*, 6369–6373.

(13) Wong, A.; Ida, R.; Spindler, L.; Wu, G. *J. Am. Chem. Soc.* **2005**, *127*, 6990–6998.

(14) Jurga-Nowak, H.; Banachowicz, E.; Dobek, A.; Patkowski, A. *J. Phys. Chem. B* **2004**, *108*, 2744–2750.

(15) Eimer, W.; Dorfmueller, T. *J. Phys. Chem.* **1992**, *96*, 6790–6800.

(16) Spindler, L.; Olenik, I. D.; Copic, M.; Romih, R.; Cerar, J.; Skerjanc, J.; Mariani, P. *Eur. Phys. J. E* **2002**, *7*, 95–102.

(17) Mariani, P.; Ciuchi, F.; Saturni, L. *Biophys. J.* **1998**, *74*, 430–435.

(18) Hightower, J. B.; Olmos, D. R.; Walmsley, J. A. *J. Phys. Chem. B* **2009**, *113*, 12214–12219.

(19) Richard, G. Weiss, P. T., *Molecular Gels: Materials with Self-Assembled Fibrillar Networks*; Springer: Dordrecht, 2006.

(20) George, M.; Funkhouser, G. P.; Terech, P.; Weiss, R. G. *Langmuir* **2006**, *22*, 7885–7893.

(21) Buhler, E.; Sreenivasachary, N.; Candau, S. J.; Lehn, J. M. *J. Am. Chem. Soc.* **2007**, *129*, 10058–10059.

(22) Buhler, E.; Boue, F. *Macromolecules* **2004**, *37*, 1600–1610.

In D<sub>2</sub>O, the labile hydrogens in TAcG and G are exchanged with deuterium which reduces the contrast between the guanine units and solvent. However, the hydrogens on the acetyl groups of the ribose ring, along with the hydrogens on the ribose unit itself, do not exchange, and thus these nonlabile hydrogens, which decorate the exterior of the cylindrical stacks, make the dominant contribution to the scattered intensity. Recognizing that the scattered intensity mainly comes from the contrast of the shell, and using eq 3, the average mass per unit length  $M_L$  (considering the shell only) was determined from Figure 2 to be  $1759 \pm 115$  (g/mol)/nm, which corresponds to an average separation distance  $d$  between quartets of  $0.44 \pm 0.03$  nm. This result is larger than that generally accepted as the typical stacking repeat of guanosine-based quartets (0.34 nm).<sup>12,23</sup> A comparable result has been reported for a similar gel formed by a lipophilic guanosine derivative<sup>21</sup> and may suggest the presence of a looser structure such as a continuous helical strand.<sup>18,24</sup>

For gels composed of rigid cylindrical rod segments, the intensity at larger  $q$  is dominated by the interferences due to the finite width of rods, and can be described using eq 4:<sup>25</sup>

$$I(q) = \frac{\phi_{vol}(\pi r \Delta\rho)^2}{q} \exp\left(-\frac{q^2 r^2}{4}\right) \quad (4)$$

where  $\phi$  is the volume fraction of rods,  $\Delta\rho$  is the scattering contrast, and  $r$  is the radius of the rodlike scatterer. Equation 4 may be rearranged in terms of the cross-sectional radius of gyration,  $R_c = r/\sqrt{2}$ , as follows:

$$I(q)q = 2\phi_{vol}(\pi R_c \Delta\rho)^2 \exp\left(-\frac{q^2 R_c^2}{2}\right) \quad (5)$$

Thus,  $R_c$  was determined from a plot of  $\ln(I(q) \times q)$  versus  $q^2$ , shown in Supporting Information, to be  $0.88 \pm 0.01$  nm. Previously, we demonstrated<sup>11</sup> that the form factor of a core-shell cylinder describes the scattering curves of the gel very well over the entire  $q$  range including the peak at highest  $q$ . The dimensions (core radius,  $R_{core} = 0.69 \pm 0.02$  nm, shell thickness,  $T_{shell} = 0.78 \pm 0.01$  nm, length:  $32.0 \pm 1.0$  nm) were previously deduced on the basis of these fits. The above value of  $R_c$  lies numerically between the value of the core radius  $R_{core}$  and total radius ( $R_{core} + T_{shell}$ ), and reflects not only the cross-sectional dimensions but also the different scattering length densities of core and shell.

**Small Angle X-ray Scattering (SAXS).** SAXS data were collected as a function of concentration up to 1.0 wt % in order to encompass the sol-gel transition. A satisfactory signal was obtained for concentrations higher than 0.5 wt % after background subtraction. The following analysis is described for G/TAcG compositions of 0.5, 0.8, and 1 wt %. The accessible lower  $q$  range was similar to earlier SANS studies ( $0.07 \text{ nm}^{-1}$ ) but was truncated at higher  $q$  ( $1.5 \text{ nm}^{-1}$  versus  $14 \text{ nm}^{-1}$ ). In the intermediate  $q$  regime ( $0.13\text{--}0.6 \text{ nm}^{-1}$ ), the scattered intensity  $I(q)$  of SAXS decreases proportionally to  $q^{-1}$ , indicative of scattering from rodlike species, as observed in SANS experiments, and demonstrated in Supporting Information. Likewise, in Supporting Information, we show Holtzer plots of  $qI(q)$  versus  $q$ , of the SAXS data, which also exhibit similar behavior to the prior

**Table 1. Dimensions from  $\ln(I(q) \times q)$  versus  $q^2$  Plot and Circular Cylinder Model Fit to SAXS Scattering Profiles of G/TAcG (50/50) at Three Concentrations**

C (wt %)	0.5	0.8	1
$R_c$ (nm)	$1.04 \pm 0.01$	$1.09 \pm 0.01$	$1.07 \pm 0.01$
$L$ (nm)	$39.9 \pm 0.3$	$39.5 \pm 0.2$	$39.7 \pm 0.1$

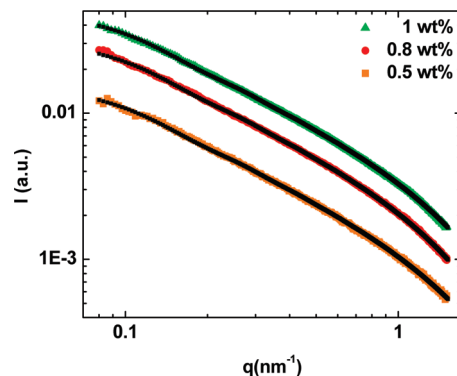


**Figure 3.** SAXS scattering profiles of G/TAcG (50/50) at three concentrations, of 0.5 (orange squares), 0.8 (red circle), and 1 (green triangle) wt %, in 0.354 M aqueous KCl and their fits to the circular cylinder model (in black).

SANS results, i.e., the presence of a plateau regime in the intermediate  $q$  range ( $0.13\text{--}0.6 \text{ nm}^{-1}$ ), again a strong indication of scattering from long rigid rods.

Following the same procedure for the SANS data analysis, according to eq 5, the cross-sectional radius of gyration,  $R_c$ , of the rods can be determined from a plot of  $\ln(I(q) \times q)$  versus  $q^2$  at large scattering vectors,  $q = 1.0\text{--}1.4 \text{ nm}^{-1}$  (shown in Supporting Information). The resulting  $R_c$  values in Table 1 are in the range  $1.05\text{--}1.09$  nm, and are a little larger than the  $R_c$  value (0.88 nm) deduced from the corresponding fits of the SANS scattering of a 2 wt % gel.<sup>11</sup> In contrast to the SANS experiments, the electron density of the core here ( $K^+$ ) is similar to that of the shell.<sup>26</sup> Thus, the values of the cylinder radius,  $r = 1.48\text{--}1.54$  nm, deduced from the above SAXS  $R_c$  results via  $r = R_c\sqrt{2}$ , are numerically comparable to the corresponding radius  $r = (R_{core} + T_{shell}) = 1.47 \pm 0.02$  nm, deduced from the SANS data via core-shell cylinder fits. From these considerations, it further follows that a solid circular cylinder form factor  $P(q)$  is found to accurately fit the SAXS patterns:

$$P(q) = \frac{\text{scale}}{V_{\text{total}}} \int_0^{\pi/2} f^2(q, \alpha) \sin \alpha \, d\alpha \quad (6)$$

where

$$f(q, \alpha) = 2(\rho_{\text{cylinder}} - \rho_{\text{solvent}}) V j_0[qL \cos \alpha/2] \frac{J_1[qR \sin \alpha]}{qR \sin \alpha} \quad (7)$$

and  $V = \pi R^2 L$ , where  $R$  is the radius of the cylinder,  $L$  is the length, and  $J_1(x)$  is the first order Bessel function.  $\alpha$  is defined as the angle between the cylinder axis and the scattering vector,  $q$ . The integral over  $\alpha$  averages the form factor over all possible orientations of the cylinder. Using  $R_c$  from  $\ln(I(q) \times q)$  versus  $q^2$  plot, the least-squares fits shown in Figure 3 leads to the cylinder lengths listed in Table 1. The lengths from the fits are comparable to those determined via SANS for the same G/TAcG composition

(23) Amaral, L. Q.; Itri, R.; Mariani, P.; Micheletto, R. *Liq. Cryst.* **1992**, *12*, 913–919.

(24) Walmsley, J. A.; Burnett, J. F. *Biochemistry* **1999**, *38*, 14063–14068.

(25) Terech, P.; Coutin, A.; Giroud-Godquin, A. M. *J. Phys. Chem. B* **1997**, *101*, 6810–6818.

(26) Mariani, P.; Spinozzi, F.; Federiconi, F.; Amenitsch, H.; Spindler, L.; Drevensek-Olenik, I. *J. Phys. Chem. B* **2009**, *113*, 7934–7944.

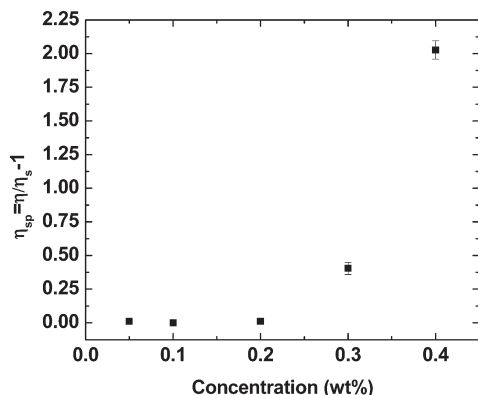


**Figure 4.** Concentration dependence of specific viscosity for **G/TAcG** (50/50) in 0.354 M aqueous KCl. A sudden increase in viscosity occurs at 0.3 wt %.

at 2 wt % ( $32.0 \pm 1.0$  nm), and do not increase with concentration consistent with the expectation that the columnar stacks of quartets have reached their asymptotic size at these concentrations.

**Viscosity Measurement.** The concentration dependence of the specific viscosity of **G/TAcG** (50/50) is exhibited in Figure 4. Solutions at concentrations up to 0.2 wt % have viscosities indistinguishable from that of the solvent within experimental error, but a dramatic increase in  $\eta_{sp}$  occurs at  $c \geq 0.3$  wt %. The reduced specific viscosity,  $\eta_{sp}/c$ , may be viewed as a measure of the apparent hydrodynamic volume,  $V_h^{app}$ , divided by the molar mass,  $M$ , of the dissolved particles:

$$\eta_{sp}/c = \left( \frac{\eta}{\eta_s} - 1 \right) / c \approx 2.5N_A \frac{V_h^{app}}{M} \quad (8)$$

Evidently, therefore, a transition point exists between 0.2 and 0.3 wt % where a rapid growth in molecular hydrodynamic volume,  $V_h$ , occurs and where the growth in  $V_h$  is much larger than the corresponding growth in molar mass. This would be consistent with the sudden appearance of rodlike particles, for which  $V_h \sim M^3$ , and hence  $\eta_{sp} \sim cV_h/M \sim n_p M^3$ , where  $n_p$  is the molar concentration of particles.

**Static Light Scattering.** To further investigate the onset of **G/TAcG** quartet self-assembly, static light scattering of 50/50 **G/TAcG** was performed in aqueous 0.354 M KCl at a series of concentrations between 0.05 to 0.8 wt %, the latter believed to be the gel point.<sup>11</sup> Using a Brice-Phoenix differential refractometer, calibrated against KCl solutions, the  $dn/dc$  value of **G/TAcG** (50/50) was determined at three different wavelengths. From the resulting plot of  $dn/dc$  versus  $1/\lambda^2$  (see Supporting Information) we determined  $dn/dc = 0.179 \pm 0.004$  mL/g at 514.5 nm. The concentration- and angle-dependence of the scattered intensity is displayed in the form of a Zimm plot in Figure 5 (see eq 15 in the Experimental Section later and details given in the Supporting Information). The weak intensity data at the two lowest concentrations show no systematic angle dependence within experimental error, indicating solute species smaller than 1/20 of the laser wavelength. Averaging the intensities at all scattering angles yields apparent weight-average molecular weights,  $M_w^{app}$ , of  $667 \pm 45$  g/mol (0.05 wt %) and  $833 \pm 185$  g/mol (0.1 wt %), each substantially smaller than the mass of a 50/50 **G/TAcG** quartet ( $M.Wt = 1385$  g/mol) but larger than that of either component (**G**, 283.24 g/mol; **TAcG**, 409.35 g/mol). At these two concentrations, it therefore appears that either species smaller than **G/TAcG** tetramers are present, or there is an equilibrium mixture

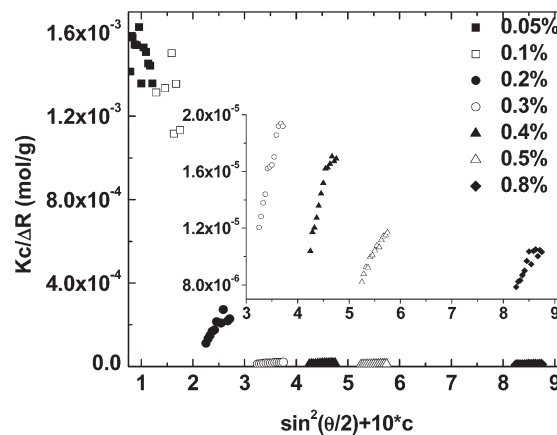


**Figure 5.** Zimm plot of **G/TAcG** 50/50 in 0.354 M aqueous KCl. Inset graph corresponds to four higher concentrations. The weak intensity data at the two lowest concentrations show no systematic angle dependence within experimental error, indicating solute species smaller than 1/20 of the laser wavelength, while at higher concentrations, the scattered intensity has significant angle dependence indicating the appearance of particles whose sizes are large compared to the laser wavelength.

of monomers, oligomers and quartets. If we assume there is only an equilibrium between monomers and quartets, and that,  $2G + 2TAcG \rightleftharpoons$  quartet, then based on the measured apparent overall molecular weights,  $M_w^{app}$ , determined via SLS, the resulting apparent overall binding constant is estimated to be ca.  $1.4 \pm 0.4 \times 10^9$  (L/mol)<sup>3</sup> (i.e., the mean of  $1.76 \times 10^9$  (L/mol)<sup>3</sup> for 0.05 wt %, and  $1.01 \times 10^9$  (L/mol)<sup>3</sup> for 0.1 wt %). For 0.2 wt % **G/TAcG**, where significant stacking of quartets already occurs, the mass fraction of quartets is estimated from this value of the overall binding constant to be  $66.7 \pm 9.0\%$ , where the error reflects the relatively high uncertainties in the two measured molecular weights.

At higher concentrations, as seen in Figure 5, the scattered intensity has significant angle dependence, indicating the appearance of particles whose sizes are large compared to the laser wavelength. Since  $qR_{g,z}^{app}$  is greater than unity using  $R_{g,z}^{app}$  values determined via Zimm plots, Guinier plots,  $\ln(Kc/\Delta R(q,c))$  versus  $q^2$ , were used to determine values of  $Kc/\Delta R(0,c)$ , whose concentration dependence is presented in the Supporting Information. Apparent weight-average molecular weights,  $M_w^{app}$ , were determined from  $Kc/\Delta R(0,c) = 1/M_w^{app}$ , and from the slopes of plots of  $\ln(Kc/\Delta R(q,c))$  versus  $q^2$ , apparent z-average radii of gyration  $R_{g,z}^{app}$  were calculated (cf. eq 16 in the Experimental Section later). The results are presented in Table 2 and indicate a dramatic increase in  $M_w^{app}$  from  $833 \pm 185$  g/mol at 0.1 wt % to  $1.78 \pm 0.03 \times 10^4$  g/mol at 0.2 wt %. This suggests that the critical concentration for stacking of **G/TAcG** quartets falls between 0.1 wt % and 0.2 wt %, where the onset of aggregation occurs.

It should be noted that the measured  $M_w^{app}$  is numerically inconsistent with the measured  $R_{g,z}^{app}$ , using accepted values of the mass per unit length  $M_L$  of columnar stacks of quartets. One source of the discrepancy arises because  $R_{g,z}^{app}$  is a z-average quantity, while  $M_w^{app}$  is a weight-average. Trace levels of large particles contribute more significantly to  $R_{g,z}^{app}$  compared to  $M_w^{app}$ . Another source of error comes from the fact that  $M_w^{app} = M_w/(1 + 2A_2M_w c + 3A_3M_w c^2)$ , where  $A_2$  and  $A_3$  are the second and third osmotic virial coefficients. Since  $A_2$  and  $A_3$  are typically positive in good solvents, this also tends to make  $M_w^{app}$  too small. Recalling that the specific viscosity measurements show a sudden

**Table 2. Apparent Weight Average Molecular Weight and Apparent  $z$ -Average Radii of Gyration for Series of Concentrations of 50/50 G/TAcG Obtained from a Guinier Plot**

G/TAcG concn (wt %)	0.2%	0.3%	0.4%	0.5%	0.8%
$M_w^{\text{app}} \times 10^5$ (g/mol)	0.178 ± 0.003	1.27 ± 0.02	1.45 ± 0.04	1.78 ± 0.05	1.55 ± 0.04
$R_{g,z}^{\text{app}}$ (nm)	100.4 ± 0.8	69.4 ± 0.9	68.4 ± 1.7	65.8 ± 2.0	47.8 ± 2.1
$qR_{g,z}^{\text{app}}$	1.5–1.8	1.1–1.3	1.1–1.4	1.1–1.2	0.8–1

increase at 0.3 wt %, it appears that the number,  $n_p$ , and/or hydrodynamic volume,  $V_h$ , of the columnar aggregates of quartets are not large enough to significantly impact the viscosity at 0.2 wt %. Thus, SLS provides a more accurate estimate of the critical concentration for quartet association. With further increase in concentration,  $M_w^{\text{app}}$  increases between 0.2 wt % to 0.3 wt %, and then reaches a plateau at  $(1.27\text{--}1.78) \pm 0.05 \times 10^5$  g/mol. Accompanying the observation of a plateau in  $M_w^{\text{app}}$ , we find that the apparent  $z$ -average radius of gyration,  $R_{g,z}^{\text{app}}$ , progressively decreases, from 100 nm at 0.2 wt % to 48 nm at 0.8 wt %. This suggests that, at these concentrations, SLS is probing intermolecular correlation length scales, which decrease with increase of concentration, i.e., that we are in the semidilute concentration regime. More detailed insight into the supramolecular organization of the columnar aggregates is obtained via DLS analysis described in the next section.

#### Polarized and Depolarized Dynamic Light Scattering.

Polarized (VV) and depolarized (VH) dynamic light scattering experiments were carried out on 50/50 G/TAcG in 0.354 M aqueous KCl as a function of concentration and scattering angle. VV and VH signals from dissolved G/TAcG only appeared for concentrations of 0.3 wt % and higher, and the electric field correlation functions  $g_{VV}^{(1)}(\tau)$  and  $g_{VH}^{(1)}(\tau)$  were each characterized by two discrete decay modes denoted as “fast” and “slow”. Typical intensity correlation functions for VV and VH scattering together with their fits to a sum of two stretched exponential decays (c.f. eq 18 in the Experimental Section later) are shown in Figure 6, parts a and b, respectively, and illustrate that, whereas the VV correlation functions showed strong angular dependence, the VH correlation functions were essentially angle-independent. CONTIN multiexponential analysis gave bimodal distributions with asymmetric distributions of decay rates, consistent with the stretched exponential decay profile of the correlations functions, and yielded similar mean decay rates to those evaluated via line shape analysis. The values of the stretched exponential exponents,  $\beta$ , were found to fall between 0.15 and 0.94. The VH fast mode  $\beta$  values (ranging between 0.15 and 0.55) are substantially smaller than the VV fast mode  $\beta$  values (ranging from 0.51 and 0.94), suggesting the former have a broader decay rate distribution. This may stem from the fact that the VH decay rates scale with particle volume whereas VV decay rates are related to particle radius. Also, for both VV and VH, there appears to be a trend toward smaller  $\beta$  values at higher concentration, suggesting the width of the decay rate distribution increases with concentration. The concentration dependence of intensity correlation functions at 90° scattering angle and their fits are shown in Supporting Information.

For each concentration, the dependence of the fitted decay rates on the scattering vector  $q$  was investigated. As an example, we show in parts a and b of Figure 7 the  $q$ -dependence of the mean decay rates of the fast and slow modes in VV and VH scattering,

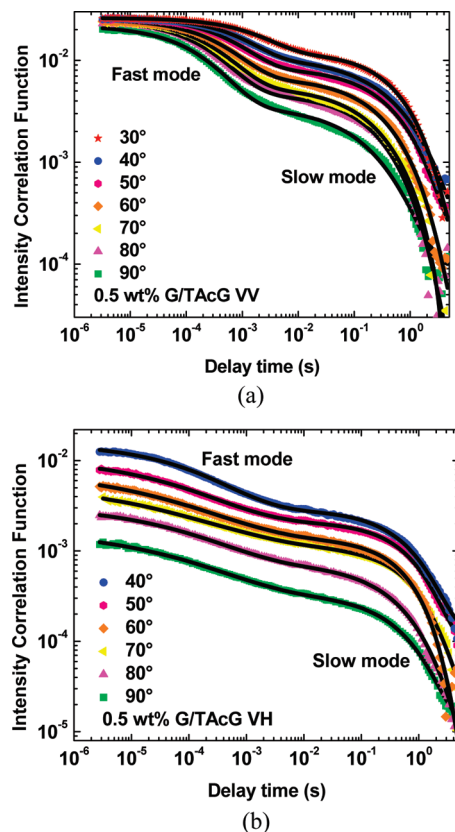


**Figure 6.** (a) Stretched exponential fit (black lines) to intensity correlation function of polarized DLS (VV) from 30° to 90° for 0.5 wt % G/TAcG (50/50) in 0.354 M aqueous KCl. (b) Stretched exponential fit (black lines) to intensity correlation function of depolarized DLS (VH) from 40° to 90° for 0.5 wt % G/TAcG (50/50) in 0.354 M aqueous KCl. Correlation functions and their fits were scaled for clarity by different factors: 0.1 for 90°; 0.2 for 80°; 0.3 for 70°; 0.4 for 60° and 0.6 for 50°. The VV correlation functions (a) show strong angular dependence suggesting translational diffusive modes, while the VH correlation functions (b) are relatively angle-independent suggesting rotational diffusion modes.

respectively, for 0.5 wt % G/TAcG (50/50) in 0.354 M aqueous KCl. It was observed that the VV fast mode decay rates were indeed proportional to  $q^2$ , indicative of scattering from translational diffusive modes. In contrast, the VH decay rates show no systematic dependence on  $q$ -vector and it is evident that the computed decay rates are relatively imprecise, reflecting the relatively weak VH scattering intensity. It is also evident that, at large  $q$ -vectors, the VH decay rates fall below the VV values, in contrast to theoretical prediction (c.f. eqs 19 and 20 in the Experimental section later). This is due to the fact that, as noted above, the VH relaxation time distributions are much wider than VV, and get wider with increasing  $q$ . Specifically, for 50/50 G/TAcG, as  $q$  increases, the  $\beta$  values decrease from 0.92 to 0.57 and from 0.46 to 0.31 for VV and VH fast modes, respectively. The smaller VH  $\beta$  values result in smaller mean decay rates, especially for higher  $q$ . The slow modes in both VV and VH have a more complex  $q$ -dependence, which reflects the fact that it is more

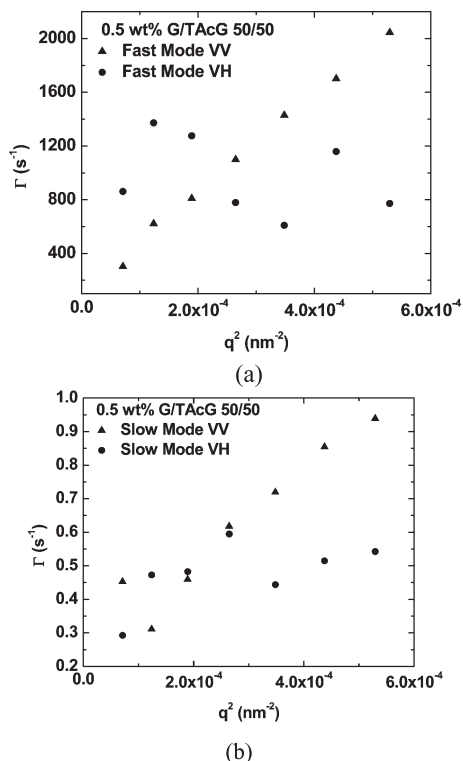


**Figure 7.** (a) Scattering vector dependence of the fast mode's decay rates for VV (solid triangles) and VH (solid circles) of 0.5 wt % G/TAcG (50/50) in 0.354 M aqueous KCl. (b) Scattering vector dependence of the slow mode's decay rates for VV (solid triangles) and VH (solid circles) of 0.5 wt % G/TAcG (50/50) in 0.354 M aqueous KCl. The data suggest a translational contribution to both the fast and slow modes in VV, while a rotational contribution exists in both modes of VH.

difficult to obtain reproducible results for the slow modes. It was difficult to obtain reliable information from the correlation functions at very long decay times, due to the low signal-to-noise ratio and the need for longer acquisition times. However, a trend toward increasing rates with increasing  $q$ -vector appears to be representative of the VV slow mode, and  $q$ -independence for the decay rate of the VH slow mode (Figure 7b). Thus, the balance of evidence suggests that these slow modes also represent translational (VV) and rotational (VH) modes, as well.

The amplitude of the slow mode in VV increases substantially relative to the fast mode as scattering angle decreases, whereas the relative contribution of each mode in VH is angle independent (see Supporting Information). It is also apparent for both VV and VH that the slow mode becomes more and more dominant as concentration increases (see Supporting Information). In principle, the slow mode may originate in microgel domains or hindered molecular motion of the rodlike aggregates, each of which reflect the approach of the system to gelation. The above static light scattering analysis indicates that we are in the semidilute concentration regime above the critical concentration (0.2 wt %). According to the Doi–Edwards<sup>27</sup> and similar theories<sup>28–30</sup> for the dynamics of rods in semidilute solution, the fast mode in VV represents unhindered longitudinal translational diffusion, and the fast mode in VH represents rotational diffusion of the rods.

The scattering vector dependences of the fast modes in VV indeed exhibit the characteristics of dominant translational diffusion. In semidilute solution, the rotational diffusion process should be more hindered and increasingly slower at higher concentrations. However, the VH fast mode is observed to be concentration independent, which suggests that it originates in scattering from rotational diffusion of rodlike aggregates in dilute solution domains. It is therefore concluded that, above the critical concentration, the system consists of coexisting dilute and microgel domains, the former giving rise to the fast modes in VV and VH dynamic light scattering, via the translation and rotation, respectively, of rodlike aggregates, while translational and rotational diffusive scattering from the microgel domains gives rise to the slow modes in VV and VH, and also makes the dominant contribution to the angular-dependence in static light scattering.

With regard to the aggregates whose scattering gives rise to the fast modes in VV and VH, it is clear that the sizes are substantially larger than those computed for the individual columnar stacks of quartets deduced from the SAXS analysis. Thus, it appears that the individual columns coexist with larger aggregates. From prior atomic force microscopy (AFM) of 40/60 and 60/40 G/TAcG gels,<sup>11</sup> the network fibers visualized have a height of 3 nm, a width of approximately 75 nm ( $\pm 25$  nm) and a persistence length of 300–600 nm. Also, from prior SANS analysis<sup>11</sup> and SAXS data presented here, the height of 3 nm is identical to the diameter of the individual columnar stacked structures formed by the G/TAcG quartets. It thus appears that lateral interactions cause the individual rods to aggregate further into these larger fibrillar structures. Additionally, it is hypothesized that a spreading process occurs in AFM sample preparation, presumably due to attraction between the individual rods and the mica surface. Using the measured fiber width of 75 nm after spreading, and assuming individual rods laterally associate into larger cylindrical structures, we estimate a diameter of 16.9 nm ( $\pm 3.0$  nm) for these larger cylinders.

The Broersma<sup>31–33</sup> equations relate  $D$  and  $\Theta$ , respectively, the translational and rotational diffusion coefficients of long rigid rods in dilute solution, to their cross-sectional diameter  $d$  and length  $L$ .

$$D = \frac{k_b T}{3\pi\eta L} \left[ \delta - \frac{1}{2}(\gamma_{\parallel} + \gamma_{\perp}) \right] \quad (9)$$

$$\delta = \ln \frac{2L}{d} \quad (10)$$

$$\gamma_{\parallel} = 0.807 + \frac{0.15}{\delta} + \frac{13.5}{\delta^2} - \frac{37}{\delta^3} + \frac{22}{\delta^4} \quad (11)$$

$$\gamma_{\perp} = -0.193 + \frac{0.15}{\delta} + \frac{8.1}{\delta^2} - \frac{18}{\delta^3} + \frac{9}{\delta^4} \quad (12)$$

$$\Theta = \frac{3k_b T}{\pi\eta L^3} (\delta - \xi) \quad (13)$$

$$\xi = 1.14 + \frac{0.2}{\delta} + \frac{16}{\delta^2} - \frac{63}{\delta^3} + \frac{62}{\delta^4} \quad (14)$$

(27) Doi, M.; Edwards, F. S. *The Theory of Polymer Dynamics*; Oxford: New York, 1986.

(28) Zero, K. M.; Pecora, R. *Macromolecules* **1982**, *15*, 87–93.

(29) Teraoka, I.; Hayakawa, R. *J. Chem. Phys.* **1988**, *89*, 6989–6995.

(30) Teraoka, I.; Hayakawa, R. *J. Chem. Phys.* **1989**, *91*, 2643–2648.

(31) Broersma, S. *J. Chem. Phys.* **1960**, *32*, 1626–1631.

(32) Broersma, S. *J. Chem. Phys.* **1960**, *32*, 1632–1635.

(33) Broersma, S. *J. Chem. Phys.* **1981**, *74*, 6989–6990.

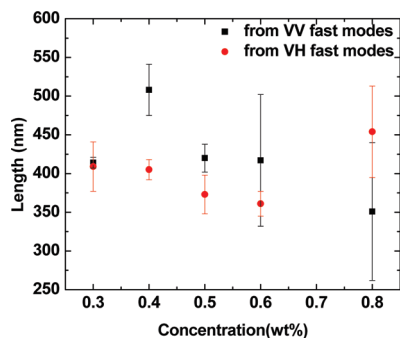


**Figure 8.** Fibrillar lengths from Broersma's relation using translational and rotational diffusion coefficients from fast mode's decay rates of VV (black squares) and VH (red circles) respectively for **G/TacG** (50/50) in 0.354 M aqueous KCl.

The fiber diameter was equated to that computed from the AFM images, and the Broersma relations for translational and rotational diffusion coefficients in dilute solutions were employed for concentrations above the critical value to extract the contour length of the rods from the fast decays. The results are displayed in Figure 8, and indicate numerically comparable values were obtained from VV and VH DLS. The contour length falls between 300 and 500 nm and is consistent with persistence lengths (300–600 nm) estimated from AFM images. It is evident that, within experimental error, the contour length remains independent of concentration above the critical concentration, which implies that the formation of microgel domains and ultimately gelation follows because of an increase in the number density of fibrils.

In summary, the SLS and DLS results suggest the coexistence of dilute (sol) and microgel domains above the critical concentration. The scattering amplitude of the microgel domains increases as the concentration increases toward the gel point ( $\sim 0.8$  wt %).

It is apparent, from the above results, that the SAXS and SANS techniques probe the same short length scale characteristics of the individual columnar stacked structures formed by the **G/TacG** quartets, which are cylindrical in shape, with a radius  $r = \sqrt{2}R_c = 1.51 \pm 0.03$  nm and a length  $L = 39.7 \pm 0.3$  nm. These techniques did not detect higher level structure because the scattering vector range did not access small enough values.<sup>34</sup> The SLS technique probes an intermediate length scale associated with fibrillar aggregates of the quartet stacks and intermolecular distances within microgel domains. Utilizing the fibrillar diameter determined via AFM ( $16.9 \pm 3.0$  nm), the polarized and depolarized DLS technique provides dimensional information on the mean length ( $411.2 \pm 45.9$  nm) of the fibrillar aggregates formed via lateral association of the columnar stacks of quartets (Figure 8). Evidently, the system is heterogeneous, featuring a sol phase with individual columnar assemblies of **G/TacG** quartets and fibrillar agglomerates and microgel domains, with the volume fraction of the latter progressively rising as the concentration increases through the macroscopic gel point.

The information gained from these SLS and DLS experiments provides a new insight into the molecular origin of the unusual viscoelastic properties of **G/TacG** gels, which feature a transient network contribution that disappears with increasing temperature.<sup>11</sup> It was noted in the earlier work that the yield stress and equilibrium modulus of the network, measured by oscillatory strain sweep at a frequency  $\omega = 10$  rad/s, decreased with increasing

**TacG** content, which correlated with the observed decrease in rod length of the individual columnar stacks, measured by SANS. At  $\omega = 10$  rad/s, the equilibrium modulus is determined by the transient network viscoelastic component. Our present results suggest that the gel network at lower temperatures consists of individual columnar quartet stacks in equilibrium with fibrillar aggregates of these stacks. It thus seems likely that the transient network contribution to the high-frequency storage modulus originates from the elastic response of the motionally restricted columnar stacks entangled within the fibrillar network, explaining the correlation between the high-frequency modulus and the rod length. It is also likely that the disappearance of the transient viscoelasticity at higher temperatures occurs because these stacks are incorporated into fibrils via hydrophobic association.

## Conclusion

In summary, SLS experiments on 50/50 w/w mixtures of guanosine (**G**) and 2',3',5'-tri-*O*-acetylguanosine (**TacG**) in aqueous 0.354 M KCl indicate a sudden increase in apparent molecular weight between 0.1 and 0.2 wt %, indicating that the critical concentration for self-association of **G/TacG** quartets into columnar assemblies is below 0.2 wt %. Guinier plot analysis of the SLS data above the critical concentration indicate a radius of gyration that decreases with concentration and smaller molecular weights than expected, suggesting that the technique is probing the internal structure of microgel particles. Polarized and depolarized DLS analyses indicate bimodal correlation functions whose properties suggest the techniques probe translational and rotational diffusion of a bimodal distribution of particles, respectively. The fast modes appear to originate from fibrillar agglomerates of columnar assemblies of **G/TacG** quartets, and the slow modes from microgel domains. SANS and SAXS measurements probe the structures of individual columnar assemblies of **G/TacG** quartets, and indicate these are described by a rigid cylindrical structure. Estimation of the mass per unit length  $M_L$  from the SANS data indicates a stacking repeat of **G/TacG** quartets of  $0.44 \pm 0.03$  nm, significantly larger than that generally accepted as typical of guanosine-based quartets (0.34 nm), suggesting the presence of a looser structure such as a continuous helical strand. The SAXS studies further indicate that the length of these rigid cylindrical assemblies is independent of concentration above the critical concentration for quartet self-assembly.

Collectively, these experiments are consistent with the interpretation that dilute sol and microgel phases coexist in the solution below the macroscopic gel point, and that the sol phase contains individual columnar stacks of **G/TacG** quartets (dimensions  $L \times d = 39.7 \pm 0.3$  nm  $\times$   $3.02 \pm 0.06$  nm) and fibrillar aggregates (dimensions  $L \times d = 411.2 \pm 45.9$  nm  $\times$   $16.9 \pm 3.0$  nm) formed via lateral aggregation of these columnar assemblies. With increasing concentration, the resulting increase in number density of rods leads to a progressive increase in the volume fraction of microgel domains and ultimately leads to macroscopic gelation. Prior observation of a transient network contribution to the gel rheology at low temperature is attributed to the presence of unassociated columnar stacks entangled within the gel network.

## Experimental Section

**Materials and Sample Preparation.** Guanosine was purchased from Sigma-Aldrich. The synthesis of 2',3',5'-tri-*O*-acetylguanosine (**TacG**) was performed according to literature procedures<sup>35</sup> and has been reported elsewhere.<sup>11</sup> For SANS

(34) Schaefer, D. W.; Rieker, T.; Agamalian, M.; Lin, J. S.; Fischer, D.; Sukumaran, S.; Chen, C. Y.; Beaucage, G.; Herd, C.; Ivie, J. J. *Appl. Crystallogr.* **2000**, *33*, 587–591.

(35) Park, T.; Todd, E. M.; Nakashima, S.; Zimmerman, S. C. *J. Am. Chem. Soc.* **2005**, *127*, 18133–18142.

measurements, stoichiometric amounts of **G/TacG** were dispersed in D<sub>2</sub>O, requiring several sonication and heating cycles to obtain a finely divided dispersion. KCl was then added at a concentration of 0.708 M to produce a solution containing 2 wt % of the guanosine moiety in 0.354 M KCl. The mixture was heated until a transparent solution was obtained, after which cooling to room temperature resulted in formation of a transparent, thermoreversible gel within a few minutes. 50/50 **G/TacG** was chosen to investigate the gelling process. A series of concentrations (0.05–1 wt %) were prepared in deionized H<sub>2</sub>O with the KCl concentration kept constant at 0.354 M for SAXS, SLS, DLS, differential refractive index increment determination, and viscosity measurements. Hot solutions were passed through polycarbonate filters (pore diameters 400 nm or 1 μm) to remove possible dust contamination, and it was confirmed via UV spectroscopy that no solute was lost during filtration.

**SANS Measurement.** SANS measurements were conducted on the time-of-flight small angle diffractometer at the Intense Pulsed Neutron Source facility of Argonne National Laboratory, Argonne, IL. The accessible range of scattering vectors  $q$  ( $q = 4\pi[\sin(\theta/2)]/\lambda$ , where  $\theta$  was the scattering angle) was very wide (0.08–14 nm<sup>-1</sup>). The neutron scattering length density of D<sub>2</sub>O was  $5.76 \times 10^{-4}$  nm<sup>-2</sup>, whereas that of **TacG** and **G** was in the range of  $(1.2\text{--}1.6) \times 10^{-4}$  nm<sup>-2</sup>. The hydrogel was contained in a quartz cell maintained at a temperature of 25 °C. Data acquisition and analysis is described elsewhere.<sup>11</sup>

**SAXS Measurement.** Small angle X-ray scattering was carried out at the BESSRC CAT 12-ID beamline of the Advanced Photon Source, Argonne National Laboratory, Argonne, IL. The setup used a sample–detector distance of 4 m and CCD detector. The sample holder was a Quarzkapillaren quartz capillary with a diameter of 2 mm purchased from the Charles Supper Company. The X-ray energy was 12 keV, corresponding to a wavelength of 0.1 nm. Small angle X-ray scattering measurements were conducted on solutions of **G/TacG** (50/50) at different concentrations. The samples were equilibrated for several hours prior to measurement. The exposure time was 1 s, and five exposures were averaged to obtain better signal quality. The signal from 0.354 M KCl solution was subtracted as background.

**Viscosity Measurement.** Cannon-Ubbelohde semimicro viscometers were used to determine the viscosity of **G/TacG** (50/50) solutions at different concentrations (0.05–0.5 wt %) following instructions on the company website.<sup>36</sup> The viscometer was maintained at 25 °C in a water bath. The ratio of the flow times of solution to solvent is an approximate measure of the relative viscosity  $\eta_r = \eta/\eta_s$ , from which the specific viscosity is obtained as  $\eta_{sp} = \eta_r - 1$ .

#### Differential Refractive Index Increment Measurement.

To obtain molecular weights from static light scattering experiments, it is necessary to know the differential refractive index increment ( $dn/dc$ ) of 50/50 **G/TacG** solutions. This was determined according to web-posted instructions written by Russo,<sup>37</sup> using a Brice-Phoenix differential refractometer as described in the Supporting Information.

**Static Light Scattering.** A Stabilite Ar<sup>+</sup> laser emitting vertically polarized light at  $\lambda = 514.5$  nm with a power output of 1–1.5 W was used for static light scattering experiments. The laser was coupled to a BI 200 SM photometer-goniometer (Brookhaven Instruments) and a BI-9000 correlator. Molecular weight determination using this light scattering instrumentation was calibrated using hydroxypropylcelluloses of known molecular weights. The scattering angle,  $\theta$ , was increased in 5° increments between 45° and 135°, corresponding to a  $q$  range from  $1.25 \times 10^{-2}$  to  $3.01 \times 10^{-3}$  nm<sup>-1</sup>. The theoretical basis for determination of weight-average molecular weight,  $M_w$ , and average radius of

gyration,  $R_g$ , via Zimm plot and Guinier plot analysis is detailed in the Supporting Information. The specific equations used to determine the apparent  $M_w^{\text{app}}$  and  $R_g^{\text{app}}$  via Zimm and Guinier plots are

$$\frac{Kc}{\Delta R(0, c)} = \frac{1}{M_w^{\text{app}}} = \frac{1}{M_w} + 2A_2c + 3A_3c^2 + \dots \quad (15)$$

and

$$\ln \frac{Kc}{\Delta R(q, c)} = \ln \frac{1}{M_w^{\text{app}}} + \frac{q^2 (R_g^{\text{app}})^2}{3} \quad (16)$$

where  $\Delta R(q, c)$  is the excess Rayleigh ratio,  $q = (4\pi/\lambda) \sin \theta$  is the scattering vector,  $c$  is concentration, and  $K$  is an optical constant, computed using the differential refractive index.

#### Polarized and Depolarized Dynamic Light Scattering.

Polarized and depolarized dynamic light scattering (DLS) experiments were carried out at scattering angles from 30 to 90° in increments of 10° using an instrument equipped with an Ar<sup>+</sup> Spectra Physics 2020 laser with power output 1.5–2W, a BI goniometer, a RCA Model 7265 photomultiplier, an ALV-5000 correlator, and a Newport RSP-2T polarizer. Particle size determination using this instrument was calibrated using polystyrene spheres and monodisperse carbon nanotubes. Methodology for determination of the mean translational ( $D_t$ ) and rotational ( $\Theta$ ) diffusion coefficients of the rodlike solute particles from the polarized and depolarized DLS correlation functions, respectively, is detailed in the Supporting Information. Briefly, the electric field correlation function can also be expressed as a Laplace transform of the normalized distribution of decay rates,  $G(\Gamma)$ :

$$g^{(1)}(\tau) = \int_0^\infty d\Gamma G(\Gamma) \exp(-\Gamma\tau) \quad (17)$$

which is equivalent to the distribution of translational diffusion coefficients,  $D_t$ , since  $\Gamma = Dq^2$ .

Several methods are available to extract information regarding  $G(\Gamma)$ . Because of its low sensitivity to noise levels, we primarily used a fitting procedure, referred to in the literature as line shape analysis,<sup>38–40</sup> which involves fitting  $g^{(1)}(\tau)$  to a sum of stretched exponentials decays, using nonlinear-least-squares simplex based minimization

$$g^{(1)}(q, \tau) = \sum_{i=1}^N A_i \exp(-\theta_i \tau^{\beta_i}) \quad (18)$$

where  $N$  is the number of relaxation modes,  $A_i$  is the amplitude of the  $i$ th mode,  $\theta_i$  is the decay pseudorate for the  $i$ th mode, and  $\beta_i$  is the stretching parameter. We found that the experimental data could be fitted to two modes and that the rms error was very small. Spectral time moments<sup>39</sup> analysis was then applied to the resulting best fit functions to determine the zeroth time moment for the  $i$ th mode which is equal the mean relaxation time,  $(\Gamma_i^{-1})$ , is equal to the zeroth time moment. While both diffusive and rotational diffusion contributes to the decay rate for VV scattering, in practice, the rotational contribution can be neglected<sup>41–44</sup> (see Supporting

(38) Streltzyk, K. A.; McKenna, J. T.; Mohieddine, R. *J. Polym. Sci., Part B: Polym. Phys.* **2008**, *46*, 771–781.

(39) Phillies, G. D. J.; O'Connell, R.; Whitford, P.; Streltzyk, K. A. *J. Chem. Phys.* **2003**, *119*, 9903–9913.

(40) Streltzyk, K. A.; McKenna, J. T. *J. Polym. Sci., Part B: Polym. Phys.* **2008**, *46*, 2792–2802.

(41) De Souza Lima, M. M.; Wong, J. T.; Paillet, M.; Borsali, R.; Pecora, R. *Langmuir* **2003**, *19*, 24–29.

(42) Berne, B. J.; Pecora, R. *Dynamic Light Scattering: With Application to Chemistry, Biology and Physics*; Dover: New York, 2000.

(43) Aragon, S. R.; Pecora, R. *J. Chem. Phys.* **1985**, *82*, 5346–5353.

(44) Claire, K.; Pecora, R. *J. Phys. Chem. B* **1997**, *101*, 746–753.

(36) <http://www.cannoninstrument.com/P10-0126%20Cannon-Ubbelohde%20Semi-Micro%20types%20instructions.pdf>.

(37) macro.lsu.edu/HowTo/dndc.doc, website of Paul Russo's Macromolecular Group, LSU.

Information). Thus, the mean diffusion coefficient,  $D_i$ , for the  $i$ th mode can be calculated from the mean decay rate as follows:

$$\langle \Gamma_i \rangle = D_i q^2 \quad (19)$$

For VH scattering, the mean rotational diffusion,  $\Theta$ , is determined by extrapolation of the mean decay rates to  $q = 0$ , since

$$\langle \Gamma_i \rangle = D_i q^2 + 6\Theta_i \quad (20)$$

In addition to line shape analysis, the normalized decay rate distribution  $G(\Gamma)$  was evaluated via an inverse Laplace transform of  $g^{(1)}(\tau)$  using CONTIN,<sup>45</sup> and produced similar results, viz. the correlation functions feature two relaxation modes with mean relaxation times comparable to those determined by the above-described line shape analysis.

---

(45) Provencher, S. W. *Makromol. Chem.* **1979**, *180*, 201–209.

**Acknowledgment.** This work was supported by the National Science Foundation Graduate Student Fellowship Program (DGE-0234629) as well as NSF Grants DMR-0513010 and CHE-0704026. We are grateful to Dr. Jyotsana Lal at Argonne National Laboratory for beam time and for her assistance in acquiring the SANS data. We also thank Krista Freeman for her help with  $dn/dc$  and SLS measurements.

**Supporting Information Available:** Figures showing plots of  $\log I(q)$  versus  $\log q$ , a plot of  $\ln(I(q) \times q)$  versus  $q^2$ , wavelength dependence of  $dn/dc$ , concentration dependence of  $Kc/\Delta R$ , stretched exponential fits to the DLS intensity correlation functions, and scattering vector (angle) dependence and text discussing the static light scattering and polarized and depolarized dynamic light scattering. This material is available free of charge via the Internet at <http://pubs.acs.org>.